ADVANCED MATERIALS
www.advmat.de

A Hierarchical Carbon Derived from Sponge-Templated Activation of Graphene Oxide for High-Performance Supercapacitor Electrodes

Jin Xu, Ziqi Tan, Wencong Zeng, Guanxiong Chen, Shuilin Wu, Yuan Zhao, Kun Ni, Zhuchen Tao, Mujtaba Ikram, Hengxing Ji, and Yanwu Zhu**

There has been an increasing demand for the development of electrochemical energy storage devices with high energy density and excellent rate performance.[1] Electrical double layer capacitors (EDLCs), also called supercapacitors (SCs), have attracted a worldwide attention owing to their long cycle lifetime and very high power density.[2–4] However, relatively low energy density (typically 3–5 W h kg^{-1}) of commercially available carbon-based SCs has significantly restricted their applications in the primary power source.[4–6]

Graphene has attracted an extensive attention in energy storage applications regarding to its unique features of high surface area, flexibility, chemical stability, excellent electric and thermal conductivity.[3,7] Graphene platelets, however, especially those derived from graphene oxide (GO) tend to agglomerate during wet-chemistry processing and are therefore leading to lower surface areas than the theoretical value of 2630 m^2 g^{-1}.[8] Strategies have been developed to assemble graphene-based platelets to 3D structures in order to prevent the restacking of platelets for higher surface areas while maintaining the intrinsic conductivity of platelets.[9] For example, Su and co-workers demonstrated a 3D macroporous bubble graphene film, in which PMMA spheres serve as the hard templates.[10] Sun and co-workers realized a sponge-templated preparation of 3D graphene sheets (STGS) with a high electrosorptive capacity of 4.95 mg g^{-1} for capacitive deionization.[11] Li et al. achieved a facile fabrication of 3D graphene networks for the decoration of silicon by employing polyurethane (PU) sponge as a template and GO as a building block.[12] Sun and co-workers prepared TiO_2-deposited reduced GO sheets using a porous PU sponge as template for photoelectrochemical oxidation of ethanol.[13] A recent study reported compressible all-solid-state SCs based on polyaniline–SWCNTs–sponge electrodes, in which sponge provides compressibility and polyaniline offers pseudocapacitance.[14]

As we can see, as a cost-effective template, sponge is able to act as an excellent support for the assembly of carbon nanostructures for SC electrodes. Sponge-templated graphene structures, however, have suffered from relatively low specific surface area (SSA) (STGS: 305 m^2 g^{-1}, for instance), which restricts the further improvement in the SC performance. On the other hand, most graphene-based assemblies with high SSAs have a low electrode density (typically <0.5 g cm^{-3}), which leads to plenty of empty space in the electrode that will be flooded by electrolyte, thereby deteriorating the performance of the final devices.[15] Li and co-workers demonstrated chemically converted graphene hydrogel films with a high packing density of up to 1.33 g cm^{-3} and simultaneously prominent capacitive performances (209 F g^{-1} and 261 F cm^{-3} in organic electrolytes).[16] The layer-like stacking of graphene platelets may deteriorate the power output due to the insufficient ion channels in the direction perpendicular to the layers.

Chemical activation is an effective method to create pores, e.g., in the preparation of activated carbons (ACs).[17] Among various chemical activation methods, KOH activation has been widely used to process graphene,[18,19] carbon nanotubes (CNTs),[20] pollens,[21] and pomelo peels[22] to deliver porosity and thus to enhance SC performances. Our research group has previously reported the fabrication of a carbon named aMEGO by KOH activation of microwave expanded graphene oxide (MEGO), from which a specific capacitance of 166 F g^{-1} in $BMIMBF_4$/AN electrolyte was achieved.[18] A direct mixture of GO suspension with KOH solution followed by drying and annealing could also lead to an activated graphene similar to aMEGO.[23] However, aMEGO also exhibits a relatively low electrode density (≈0.35 g cm^{-3}), which has largely reduced its volumetric performance.[24] Transforming low-density carbons to an assembly with a practically useful density yet with a relatively high porosity and high electrical conductivity is expected to practically useful SCs, especially when it is compatible to high-voltage organic electrolytes.

In this work, a 3D hierarchical carbon is prepared by combining sponge-templating with KOH activation of GO platelets. It is found that the sponge assembles GO platelets around its backbone, while KOH suctioned inside the sponge creates a huge number of micropores in backbone during the thermal annealing, leading to a highly conductive yet highly porous carbon. Due to the shortened ion transport distance in the 3D hierarchical and inner porous structure, an excellent

J. Xu, Z. Tan, W. Zeng, G. Chen, S. Wu, Y. Zhao, K. Ni, Z. Tao, M. Ikram, Prof. H. Ji, Prof. Y. Zhu
Key Laboratory of Materials for Energy Conversion
Chinese Academy of Sciences
Department of Materials Science and Engineering
University of Science and Technology of China
96 Jin Zhai Rd, Anhui Province, Hefei 230026, P. R. China
E-mail: jihengx@ustc.edu.cn; zhuyanwu@ustc.edu.cn
Prof. H. Ji, Prof. Y. Zhu
iChEM (Collaborative Innovation Center
of Chemistry for Energy Materials)
University of Science and Technology of China
96 Jin Zhai Rd, Anhui Province, Hefei 230026, P. R. China

DOI: 10.1002/adma.201600586

© 2016 WILEY-VCH Verlag GmbH & Co. KGaA, Weinheim

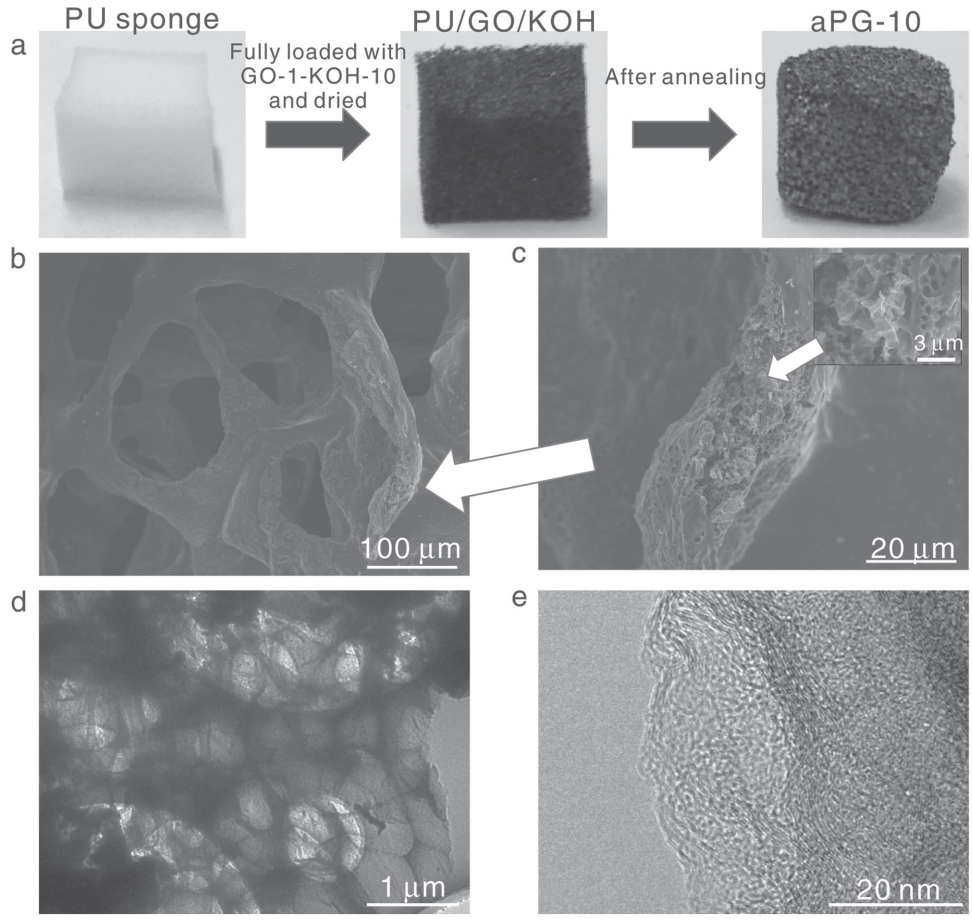

Figure 1. a) Schematic of the preparation for aPG-10. b,c) SEM images and d,e) TEM images of as-prepared aPG-10. The inset in (c) is a magnified image of the cross-section of the skeleton.

electrochemical behavior with a high specific capacitance (of up to 401 F g^{-1} in aqueous electrolytes measured in three-electrode configuration, 207 F g^{-1} and 149 F cm^{-3} in organic electrolytes measured in two-electrode configuration) has been obtained, resulting in high energy density and high power density.

Preparation of the 3D hierarchical carbon (aPG-10) is briefly illustrated in the **Figure 1**a and a detailed experimental description is provided in Supporting Information. Typically, a piece of PU sponge was immersed into a homogeneous suspension named as GO-1-KOH-10 (1 mg mL^{-1} GO mixed with 10 mg mL^{-1} KOH) and repeatedly squeezed/released for a complete suction. Afterwards, the sponge was lifted out and dried to obtain a PU/GO/KOH mixture. The weight gains of sponge with bare KOH solution, bare GO suspension or mixed suspension have been recorded to verify the homogeneous suction of GO and KOH in the sponge, as shown in Table S1 in the Supporting Information. The dried PU/GO/KOH mixture was annealed at 900 °C for 2 h in argon flow and subjected to washing and drying, leading to a final sample named as aPG-10. PG-0, aPG-2, aPG-5, and aPG-20 were fabricated from the suspensions of GO-1 (1 mg mL^{-1} GO), GO-1-KOH-2 (1 mg mL^{-1} GO mixed with 2 mg mL^{-1} KOH), GO-1-KOH-5 (1 mg mL^{-1} GO mixed with 5 mg mL^{-1} KOH), GO-1-KOH-20 (1 mg mL^{-1} GO mixed with 20 mg mL^{-1} KOH), respectively, following the same process with that for aPG-10. In control experiments, pure PU sponges or dried mixture of PU/KOH solution (with a concentration of from 2 to 20 mg mL^{-1}) has been annealed with the same procedures, but no products could be obtained without the existence of GO platelets, indicating that sponge has been completely pyrolyzed during the annealing process. On the other hand, a certain amount of GO-1 or GO-1-KOH-10 suspension was directly dried without the existence of sponge at 60 °C and treated in the same process to obtain rGO or aGO-10 as references.

The morphology of as-prepared aPG-10 was examined by scanning electron microscopy (SEM). Figure 1b shows that aPG-10 owns a well-defined interconnected porous structure, similar to that of pure sponge without any processing as shown in Figure S1 in the Supporting Information. By zooming into inside the 3D structure (Figure 1c), the surface of the skeleton looks smooth while a large amount of honeycomb-like pores (about 0.9 μm in diameter, as shown in Figure S2 in the Supporting Information) are observed in the broken cross-section of skeleton, as shown in the inset of Figure 1c. The hierarchical structure can be observed more clearly with transmission electron microscopy (TEM). As can be seen from Figure 1d, the skeleton consists of plentiful pores which is covered with a thin membrane. The image with higher magnification (Figure 1e)

© 2016 WILEY-VCH Verlag GmbH & Co. KGaA, Weinheim
Adv. Mater. **2016**,
DOI: 10.1002/adma.201600586

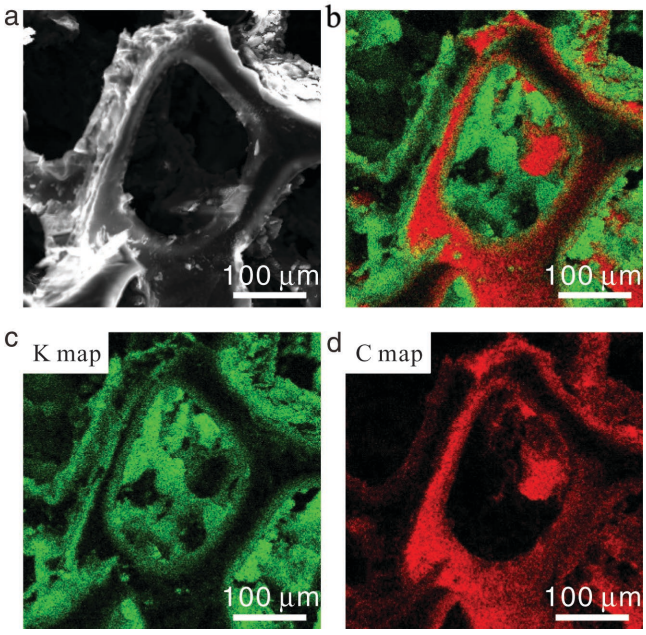

Figure 2. a) SEM images of dried mixture of sponge with GO-1-KOH-10 suspensions. b–d) Its EDS mappings of overlayed elements (b), K element (c), and C element (d).

shows the amorphous feature of the carbon with micropores in the skeleton, similar to previous observations in ACs or activated graphene materials.[6,18,21,25,26] Such porous structure of aPG-10 has made it very fragile, leading to a low Young's modulus of ≈0.04 MPa and a yield strength of ≈0.005 MPa, measured by a compression test.

Obviously aPG-10 has copied the macroporous structure of sponge while micropores and mesopores are introduced in KOH activation. To have the hint for the formation mechanism of the porous skeleton covered with a relatively smooth surface in aPG-10, elemental mapping was performed by energy dispersive spectrometer (EDS), as presented in **Figure 2**, to reveal the elemental distribution in the PU/GO/KOH dry mixture before annealing (activation) at 900 °C. Figure 2a shows the SEM image of the mixture, from which macroscopic pores with sizes similar to those in aPG-10 are observed, verifying that the 3D aPG-10 network is generated due to the sponge-templating. As shown in Figure 2b–d, the C element distributes on the whole surface of the skeleton in the sponge, where K signals could be hardly observed. Instead, abundant K has been found inside the backbone of the skeleton, as shown in Figure 2c. Such a distribution of K element may be explained by the existence of numerous pores in the backbone of the sponge, which may agglomerate more KOH by capillary force but block big GO platelets out of the skeleton during drying. The distribution of GO and KOH in the dried PU/GO/KOH mixture is illustrated in Schematic S1 in the Supporting Information as well. Thus, during the annealing at 900 °C, the KOH activation would start from the inside of skeleton, leading to the formation of the microporous structure.[18,27] At the same time, those GO platelets covering the surface of skeletons remain more intact, forming the unique morphology in aPG-10. Without KOH, as in the case of PG-0, a network with hollow skeletons of reduced GO was obtained, as indicated in Figure S3 in the Supporting Information and previous work.[28] Compared to the morphology of rGO and aGO-10 (Figure S4, Supporting Information), the sponge-templating in the preparation of aPG-10 has effectively prevented the collapse or agglomeration of GO platelets.[11,13,28] As a result, a 3D hierarchical carbon with reduced GO covering on the skeleton and simultaneously a large amount of mesopores and micropores developed inside the skeleton have been obtained by simply combining the sponge-templating and KOH activation in one process.

SEM images of samples obtained from various KOH/GO ratios (aPG-2, aPG-5, and aPG-20) are shown in Figure S4 in the Supporting Information as well. Generally, more pores in the skeleton are observed with increase in the amount of KOH. With less KOH in the mixtures, aPG-2 and aPG-5 do not exhibit honeycomb-like porous backbones but an intact 3D network. On the other hand, the surface of aPG-20, obtained from the mixture with excess amount of KOH, is dotted with plenty of fractures even if the porous backbone survives. Moreover, the yield of aPG-20 is lower than 5%, which limits the further investigations.

N_2 adsorption–desorption measurements were carried out to further investigate the micropores and mesopores in aPG-10, as shown in **Figure 3**a. The pore size distribution calculated from adsorption data using a quenched solid density functional theory (QSDFT) method reveals that the pore size distribution of aPG-10 is concentrated upon micropores with a range of 0.48–4 nm, whilst aGO-10 shows a wider range of 0.9–12 nm, indicating that sponge-templating plays a role in the narrowed distribution of pores. A series of pore size distributions from more samples are shown in Figure S6 in the Supporting Information. By comparing the SSA of PG-0 (the sample without KOH) and those of aPG samples, we can clearly see that the porosity and SSA in aPG samples has been increased by KOH activation. aPG-10 possesses a SSA of 2582 $m^2 g^{-1}$, which is two times higher than that of aGO-10 (1165 $m^2 g^{-1}$). We attribute the improvement in the SSAs to the role of sponge-templating, which has prevented the aggregation of GO platelets[13] and the pyrolysis of sponge could also helped the creation of pores. SSA increases with the content of KOH for aPG samples studied, while PG-0 exhibits a very low SSA of 17.8 $m^2 g^{-1}$.

X-ray diffraction (XRD) is shown in Figure 3b. Two weak and broad peaks at about $2\theta = 24°$ and 43° are attributed to the (002) and (100) reflections of graphitic carbon layers, respectively. The high intensity in the low angle region results from the existence of abundant micropores in the aPG samples.[18] Peak width of (002) in aPG samples has been dramatically broadened by porous structure. By comparing the spectra of aPG-10 and aGO-10, we can see the sponge-templating might be more effective to interlayer-distance control as the spectrum of aGO-10 shows the most broadened (002) peak. The Raman spectra in Figure S7 in the Supporting Information further reveal the amorphous structure of aPG samples. The peaks observed at 1349 and 1590 cm^{-1} are the D(defects and disorder) and G(graphitic) bands of carbon materials respectively. All D/G intensity ratios of PG-0, aPG-2, aPG-5, aPG-10, and aGO-10 are about 1, indicating the similar level of amorphous carbon/defects in the samples.[22]

© 2016 WILEY-VCH Verlag GmbH & Co. KGaA, Weinheim

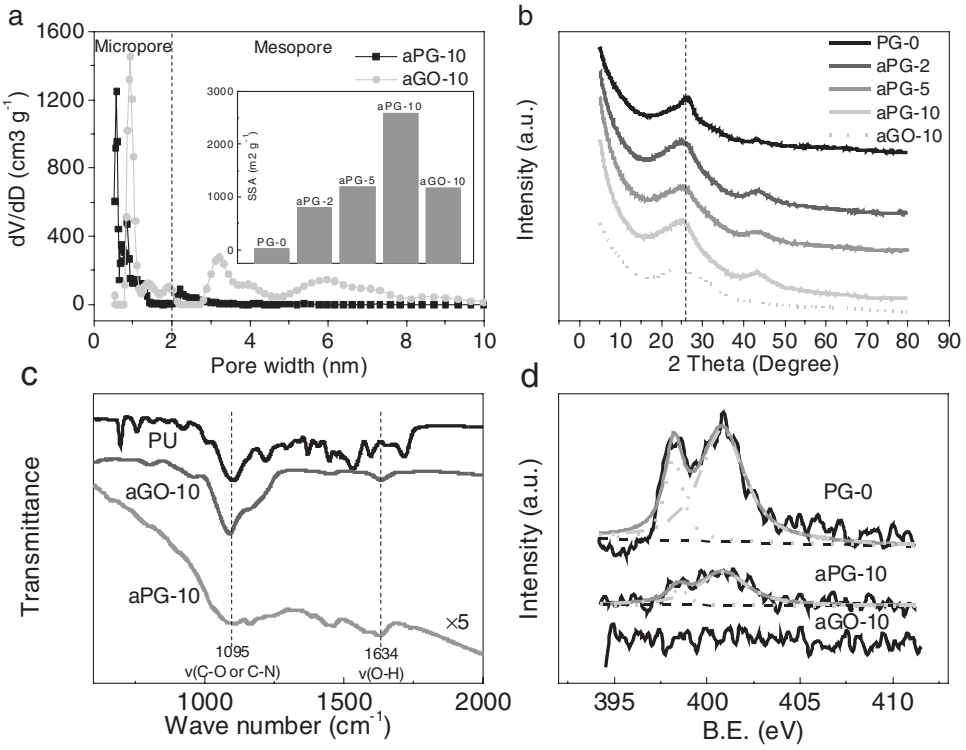

Figure 3. a) Pore-size distribution of aPG-10 and aGO-10 from nitrogen adsorption. The inset in (a) shows the SSA. b) XRD spectra of PG-0, aPG-2, aPG-5, aPG-10, and aGO-10. c) FTIR spectra of PU sponge, aGO-10, and aPG-10. d) XPS N 1s spectra of PG-0, aGO-10, and aPG-10.

Fourier transform infrared (FTIR) spectroscopy was applied to examine the functional groups in PU sponge, PG-0, aGO-10, and aPG-10, and check whether the PU sponge had been totally pyrolyzed by the annealing process. In the spectra shown in Figure 3c, the broad peak at 1620 cm^{-1} is attributed to the O–H vibrations of water absorbed on the surface of samples. Another broad band at about 1100 cm^{-1} stems from the C–O or C–N stretching vibration.[22] As can be seen, the spectrum of aPG-10 agrees well with that of aGO-10, totally contrary to that of PU sponge. The peaks observed from 650 to 1800 cm^{-1} in PU sponge disappear from aGO-10 and aPG-10, indicating the complete pyrolysis of the sponge in the activation process.[11,13] X-ray photoelectron spectroscopy (XPS) spectra are illustrated in Figure 3d and elemental compositions of these samples are shown in Table S2 in the Supporting Information, in which aPG-10 has a nitrogen content of 1.27 at%. We can clearly see the existence of N in aPG-10 and PG-0, while no N signal is found from aGO-10. This result suggests that PU sponge has introduced N-doping in aGO samples;[11] the proportion of N decreases with the increase in KOH in the mixture before annealing. The N1s spectra of aPG-10 and PG-0 display two peaks centered at 398.2 and 400.8 eV, corresponding to pyridinic and graphitic N, respectively. One pyridinic N atom is bonded with two sp^2 C atoms and provides one pair of electrons to the π system, thus inducing electron donor properties to the carbon layers.[22] The graphitic N atom doped inside the aromatic ring delivers a positive charge and electron acceptor, which enhances the conductivity of aPG-10.[29] Table S3 in the Supporting Information shows the square resistances of membranes made from samples; aPG-10 shows a much lower value of 2.41 Ω sq^{-1}, compared with rGO and aGO-10. Besides, the N atoms doped into carbon networks may enhance the wettability of electrode interface to electrolyte, and produce affluent faradic pseudocapacitance in aqueous electrolytes.[30]

The performance of the aPG-10 as an electrode material for SCs was investigated using cycle voltammetry (CV) and galvanostatic charge–discharge (GCD). **Figure 4**a,b show the performance of aPG-10 electrode coated on glassy carbon in a three-electrode configuration with 1.0 M H_2SO_4 as electrolyte. The specific capacitance calculated from the discharge at a current density of 5 A g^{-1} is 401 F g^{-1}, which remains 349 F g^{-1} at a current density of 100 A g^{-1}. When aPG-10 was tested in 6.0 M KOH electrolyte, a specific capacitance of 227 F g^{-1} at 5 A g^{-1} was obtained in the three-electrode configuration, as shown in Figure S8 in the Supporting Information. Previous work reported that the conductivity and wettability of graphene sheets can be improved by nitrogen doping, leading to a considerable benefit to the application for SCs.[22,32] The N doping in aPG-10 should play such a role,[33] as proposed with a N-H redox mechanism in acidic condition.[34] Compared with porous carbon materials previously reported, aPG-10 is a very competitive electrode material in aqueous electrolytes, as shown in Table S4 in the Supporting Information. Notably, the specific capacitance and rate ability of aPG-10 shows a mass loading dependence in three-electrode measurements, in both KOH and H_2SO_4 electrolytes (inset of Figure 4b and Figure S9, Supporting Information), which could be related to the change in internal resistance and in ion diffusion for electrodes with different loadings.

© 2016 WILEY-VCH Verlag GmbH & Co. KGaA, Weinheim
Adv. Mater. 2016,
DOI: 10.1002/adma.201600586

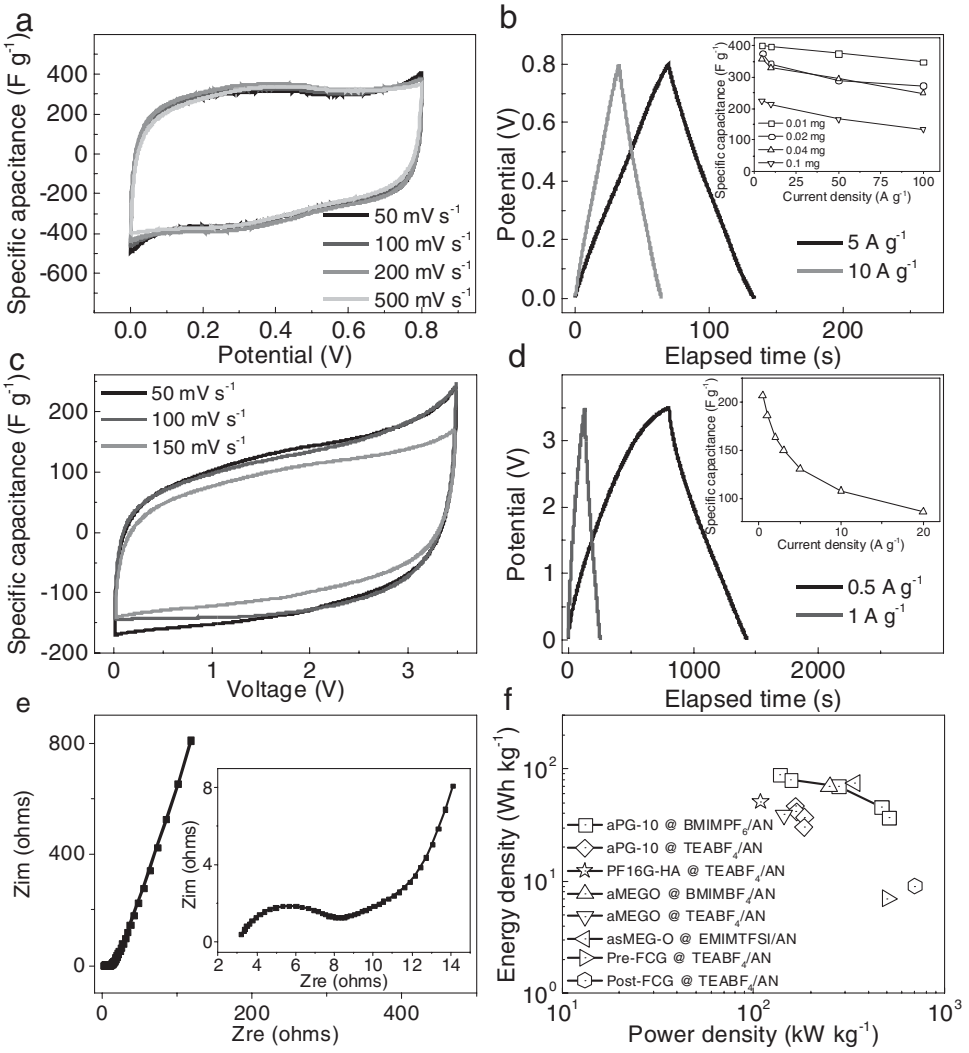

Figure 4. a) Cyclic voltammetry curves for scan rates of from 50 to 500 mV s^{-1} in 1.0 M H_2SO_4 measured in a three-electrode configuration. b) Galvanostatic charge/discharge curves under different constant currents in 1.0 M H_2SO_4. The inset shows the rate ability with increased mass loading on glassy carbon electrode. c) Cyclic voltammetry curves for different scan rates from 50 to 150 mV s^{-1} in 1.0 M $BMIMPF_6$/AN in a two-electrode configuration. d) Galvanostatic charge/discharge curves at constant currents of 0.5 and 1 A g^{-1} in 1.0 M $BMIMPF_6$/AN. The inset shows the specific capacitance calculated at various current densities. e) Nyquist plot showing the imaginary part versus the real part of impedance in 1.0 M $BMIMPF_6$/AN. Inset magnifies the data in the high-frequency range. f) Ragone plots of aPG-10 electrode in 1.0 M $BMIMPF_6$/AN and 1.0 M $TEABF_4$/AN, compared with aMEGO,[18] asMEG-O,[6] PF16G-HA,[26] pre-FCG,[31] and post-FCG.[6]

Two-electrode symmetrical coin cells have also been assembled to evaluate aPG-10 in 1-butyl-3-methylimidazolium hexafluorophosphate ($BMIMPF_6$), tetraethylammonium tetrafluoroborate ($TEABF_4$) electrolytes in acetonitrile (AN) or 6.0 M KOH aqueous electrolyte, by using the best-practice method.[35] Figure 4c demonstrates the CV curves for the voltage of from 0 to 3.5 V with scan rates varying from 50 to 150 mV s^{-1} in $BMIMPF_6$/AN. All curves exhibit quasi-rectangular shapes, showing the behavior of an electrical double-layer capacitor. The GCD curves in Figure 4d show good symmetry and nearly linear discharge slopes, indicating the feature of electrical double layer capacitors as well. The voltage drop at the beginning of the discharge curve is only 0.022 V for the current density of 0.5 A g^{-1} and corresponds to a low equivalent series resistance (ESR) of 0.044 Ω. From the discharge curves, the specific capacitance was calculated as 207, 186, 163, 149 131, 107 F g^{-1} at current densities of 0.5, 1, 2, 3, 5, and 10 A g^{-1}, respectively, as summarized in the inset of Figure 4d. Figure S8 and S10 in the Supporting Information show that aPG-10 symmetric electrodes in 6.0 M KOH aqueous electrolyte or 1.0 M $TEABF_4$/AN demonstrate a specific capacitance of 188 F g^{-1} or 126 F g^{-1} at 1 A g^{-1}, respectively. According to the density of electrodes (0.72 g cm^{-3} for aPG-10, shown in Figure S10 in the Supporting Information), a volumetric capacitance of 149 F cm^{-3} is obtained in $BMIMPF_6$/AN. Such a value is higher than those of commercially used ACs and comparable to or even higher than the best reported values for other porous carbon-based electrode materials (in most cases, with a density of 0.3–0.6 g cm^{-3}).[6,22,36] As shown in Figure S11 in the Supporting Information, a balance between density and porosity has been

© 2016 WILEY-VCH Verlag GmbH & Co. KGaA, Weinheim

reached in aPG-10 among all samples. Figure 4e shows the Nyquist plot obtained from electrochemical impedance spectroscopy (EIS) in the frequency range of 0.01 Hz to 100 kHz, and a magnified view of the curve in the high-frequency region in the inset. From the plots we can see that aPG-10 demonstrates a nearly ideal capacitive behavior with a vertical slope at the low-frequency region and an ionic resistance of as small as 3.16 Ω. The cycling test shows that the electrode has a retention of 93% in capacitance in $BMIMPF_6$/AN at 10 A g^{-1} after 4000 times of charging/discharging.

The energy storage performance of symmetric SCs assembled with aPG-10 as the electrode is shown in the Figure 4f, by comparing with previous works based on aMEGO[18] with BMIMBF4/AN and TEABF4/AN electrolyte, asMEGO[6] with EMIMTFSI/AN electrolyte, PF16G-HA[26] with $TEABF_4$/AN electrolyte, Pre-FCG[31] and Post-FCG[31] with $TEABF_4$/AN electrolyte. Benefiting from the high specific capacitance of up to 207 F g^{-1} (in $BMIMPF_6$/AN at a current density of 0.5 A g^{-1}) and an operating voltage of 3.5 V, aPG-10 exhibits a high energy density of ≈89 W h kg^{-1} (≈64 W h L^{-1}) at a power density of ≈99 kW kg^{-1} (≈71 kW L^{-1}), and a high power density of ≈512 kW kg^{-1} (≈369 kW L^{-1}) at an energy density of ≈36.54 W h kg^{-1} (≈26 W h L^{-1}). The overall performance of aPG-10 is comparable and even superior to those previously reported porous carbon materials, as summarized in Table S5 in the Supporting Information. In addition, the areal capacitance of aPG-10 is calculated to be 15.53 μF cm^{-2} in 1.0 M H_2SO_4 by normalizing to the SSA. It was reported that the areal capacitance of single-layer graphene is 13.5 μF cm^{-2};[37] the higher specific capacitance in aPG-10 could be explained by specifically designed structure and N-doping in this work.[29] The mesopores and macropores could provide electrolyte ion transportation and diffusion channels in 3D while abundant micropores serves as great candidates for ion storage.[38] Simultaneously, the reduced GO platelets on the surface of skeleton offer highly conductive channels for electron transport and lowers the square resistance of the prepared electrodes. It is worth noting that the specific capacitance from three-electrode measurements is lower than that from two-electrode measurements, even using the same electrode membranes and the same electrolyte (e.g., in 6.0 M KOH, as shown in Figure S9 in the Supporting Information), which could be explained by the difference in the current collector and testing methodology.[35]

In summary, a hierarchical porous carbon was fabricated by an "activation from the inside out" method. The sponge has served as an efficient template to suction KOH into its backbone and simultaneously assemble GO platelets into a 3D structure. After the activation process, a 3D architecture in which plentiful honeycomb-like meso- and micropores were covered by a chiffon-like 3D graphene membrane has been obtained. Low sheet resistance, high BET specific surface area, and practically acceptable electrode density have been realized based on the carbon. All these merits lead to the excellent electrochemical performance of the carbon electrodes.

Supporting Information

Supporting Information is available from the Wiley Online Library or from the author.

Acknowledgements

Y.Z. appreciates the financial support from China Government 1000 Plan Talent Program, China MOE NCET Program, Natural Science Foundation of China (51322204), the Fundamental Research Funds for the Central Universities (WK2060140014 and WK2060140017), and the External Cooperation Program of BIC, Chinese Academy of Sciences (211134KYSB20130017). H.J. appreciates the financial support from Natural Science Foundation of China (21373197), the 100 Talents Program of the Chinese Academy of Sciences, and the Fundamental Research Funds for the Central Universities (WK2060140018 and WK3430000003).

Received: January 30, 2016
Published online:

[1] a) J. Liu, *Adv. Funct. Mater.* **2013**, *23*, 924; b) P. Simon, Y. Gogotsi, *Nat. Mater.* **2008**, *7*, 845; c) J. Liu, J. G. Zhang, Z. G. Yang, J. P. Lemmon, C. Imhoff, G. L. Graff, L. Y. Li, J. Z. Hu, C. M. Wang, J. Xiao, G. Xia, V. V. Viswanathan, S. Baskaran, V. Sprenkle, X. L. Li, Y. Y. Shao, B. Schwenzer, *Adv. Funct. Mater.* **2013**, *23*, 929; d) S. Chu, A. Majumdar, *Nature* **2012**, *488*, 294.
[2] L. Hao, X. Li, L. Zhi, *Adv. Mater.* **2013**, *25*, 3899.
[3] J. Yan, Q. Wang, T. Wei, Z. Fan, *Adv. Energy Mater.* **2014**, *4*, 1300816.
[4] A. Burke, *J. Power Sources* **2000**, *91*, 37.
[5] A. Burke, *Electrochim. Acta* **2007**, *53*, 1083.
[6] T. Kim, G. Jung, S. Yoo, K. S. Suh, R. S. Ruoff, *ACS Nano* **2013**, *7*, 6899.
[7] J. Zhu, D. Yang, Z. Yin, Q. Yan, H. Zhang, *Small* **2014**, *10*, 3480.
[8] X. Yang, J. Zhu, L. Qiu, D. Li, *Adv. Mater.* **2011**, *23*, 2833.
[9] X. H. Cao, Z. Y. Yin, H. Zhang, *Energy Environ. Sci.* **2014**, *7*, 1850.
[10] C. M. Chen, Q. Zhang, C. H. Huang, X. C. Zhao, B. S. Zhang, Q. Q. Kong, M. Z. Wang, Y. G. Yang, R. Cai, D. Sheng Su, *Chem. Commun.* **2012**, *48*, 7149.
[11] Z. Y. Yang, L. J. Jin, G. Q. Lu, Q. Q. Xiao, Y. X. Zhang, L. Jing, X. X. Zhang, Y. M. Yan, K. N. Sun, *Adv. Funct. Mater.* **2014**, *24*, 3917.
[12] B. Li, S. B. Yang, S. M. Li, B. Wang, J. H. Liu, *Adv. Energy Mater.* **2015**, *5*, 1500289.
[13] L. Jing, H. L. Tan, R. Amal, Y. H. Ng, K. N. Sun, *J. Mater. Chem. A* **2015**, *3*, 15675.
[14] Z. Niu, W. Zhou, X. Chen, J. Chen, S. Xie, *Adv. Mater.* **2015**, *27*, 6002.
[15] Y. Gogotsi, P. Simon, *Science* **2011**, *334*, 917.
[16] X. Yang, C. Cheng, Y. Wang, L. Qiu, D. Li, *Science* **2013**, *341*, 534.
[17] a) H. Marsh, F. R. Reinoso, *Activated Carbon*, Elsevier **2006**; b) J. C. Wang, S. Kaskel, *J. Mater. Chem.* **2012**, *22*, 23710.
[18] Y. Zhu, S. Murali, M. D. Stoller, K. J. Ganesh, W. Cai, P. J. Ferreira, A. Pirkle, R. M. Wallace, K. A. Cychosz, M. Thommes, D. Su, E. A. Stach, R. S. Ruoff, *Science* **2011**, *332*, 1537.
[19] X. Zhao, L. Zhang, S. Murali, M. D. Stoller, Q. Zhang, Y. Zhu, R. S. Ruoff, *ACS Nano* **2012**, *6*, 5404.
[20] E. Raymundo-Piñero, P. Azaïs, T. Cacciaguerra, D. Cazorla-Amorós, A. Linares-Solano, F. Béguin, *Carbon* **2005**, *43*, 786.
[21] L. Zhang, F. Zhang, X. Yang, K. Leng, Y. Huang, Y. Chen, *Small* **2013**, *9*, 1342.
[22] Q. Liang, L. Ye, Z. H. Huang, Q. Xu, Y. Bai, F. Kang, Q. H. Yang, *Nanoscale* **2014**, *6*, 13831.
[23] L. L. Zhang, X. Zhao, M. D. Stoller, Y. Zhu, H. Ji, S. Murali, Y. Wu, S. Perales, B. Clevenger, R. S. Ruoff, *Nano Lett.* **2012**, *12*, 1806.
[24] S. Murali, N. Quarles, L. L. Zhang, J. R. Potts, Z. Q. Tan, Y. L. Lu, Y. W. Zhu, R. S. Ruoff, *Nano Energy* **2013**, *2*, 764.
[25] L. L. Zhang, X. Zhao, M. D. Stoller, Y. Zhu, H. Ji, S. Murali, Y. Wu, S. Perales, B. Clevenger, R. S. Ruoff, *Nano Lett.* **2012**, *12*, 1806.
[26] L. Zhang, F. Zhang, X. Yang, G. Long, Y. Wu, T. Zhang, K. Leng, Y. Huang, Y. Ma, A. Yu, Y. Chen, *Sci. Rep.* **2013**, *3*, 1408.

© 2016 WILEY-VCH Verlag GmbH & Co. KGaA, Weinheim

[27] C. Portet, M. A. Lillo-Rodenas, A. Linares-Solano, Y. Gogotsi, *Phys. Chem. Chem. Phys.* **2009**, *11*, 4943.
[28] B. Li, S. B. Yang, S. M. Li, B. Wang, J. H. Liu, *Adv. Energy Mater.* **2015**, *5*, 1500289.
[29] Z. Li, Z. W. Xu, H. L. Wang, J. Ding, B. Zahiri, C. M. B. Holt, X. H. Tan, D. Mitlin, *Energy Environ. Sci.* **2014**, *7*, 1708.
[30] G. Hasegawa, T. Deguchi, K. Kanamori, Y. Kobayashi, H. Kageyama, T. Abe, K. Nakanishi, *Chem. Mater.* **2015**, *27*, 4703.
[31] L. J. Wang, M. F. El-Kady, S. Dubin, J. Y. Hwang, Y. L. Shao, K. Marsh, B. McVerry, M. D. Kowal, M. F. Mousavi, R. B. Kaner, *Adv. Energy Mater.* **2015**, *5*, 1500786.
[32] B. You, L. Wang, L. Yao, J. Yang, *Chem. Commun.* **2013**, *49*, 5016.
[33] Y. Qin, J. Yuan, J. Li, D. Chen, Y. Kong, F. Chu, Y. Tao, M. Liu, *Adv. Mater.* **2015**, *27*, 5171.
[34] T. Lin, I.-W. Chen, F. Liu, C. Yang, H. Bi, F. Xu, F. Huang, *Science* **2015**, *350*, 1508.
[35] M. D. Stoller, R. S. Ruoff, *Energy Environ. Sci.* **2010**, *3*, 1294.
[36] a) X. L. Yu, J. G. Wang, Z. H. Huang, W. C. Shen, F. Y. Kang, *Electrochem. Commun.* **2013**, *36*, 66; b) M. Ghaffari, Y. Zhou, H. Xu, M. Lin, T. Y. Kim, R. S. Ruoff, Q. M. Zhang, *Adv. Mater.* **2013**, *25*, 4879; c) J. Luo, H. D. Jang, J. Huang, *ACS Nano* **2013**, *7*, 1464; d) C. Zhang, W. Lv, Y. Tao, Q. H. Yang, *Energy Environ. Sci.* **2015**, *8*, 1390.
[37] a) H. Ji, X. Zhao, Z. Qiao, J. Jung, Y. Zhu, Y. Lu, L. L. Zhang, A. H. MacDonald, R. S. Ruoff, *Nat. Commun.* **2014**, *5*, 3317; b) J. Chmiola, G. Yushin, Y. Gogotsi, C. Portet, P. Simon, P. L. Taberna, *Science* **2006**, *313*, 1760.
[38] a) Y. Li, Z. Y. Fu, B. L. Su, *Adv. Funct. Mater.* **2012**, *22*, 4634; b) D. R. Rolison, J. W. Long, J. C. Lytle, A. E. Fischer, C. P. Rhodes, T. M. McEvoy, M. E. Bourg, A. M. Lubers, *Chem. Soc. Rev.* **2009**, *38*, 226; c) S. Han, D. Wu, S. Li, F. Zhang, X. Feng, *Adv. Mater.* **2014**, *26*, 849.

© 2016 WILEY-VCH Verlag GmbH & Co. KGaA, Weinheim